Natural Resources Canada | Ressources naturelles Canada

GEOLOGICAL SURVEY OF CANADA
OPEN FILE 9310e

Electromagnetic surveys for talik investigations, First Landing and Second Landing lakes, Rankin Inlet, Nunavut

G.A. Oldenborger

2026

Canada

GEOLOGICAL SURVEY OF CANADA
OPEN FILE 9310e

Electromagnetic surveys for talik investigations, First Landing and Second Landing lakes, Rankin Inlet, Nunavut

G.A. Oldenborger

2026

Recommended citation
Oldenborger, G.A., 2026. Electromagnetic surveys for talik investigations, First Landing and Second Landing lakes, Rankin Inlet, Nunavut; Geological Survey of Canada, Open File 9310e, 26 p. https://doi.org/10.4095/pe2sqmjwm5

Publications in this series have not been edited; they are released as submitted by the author.

ISSN 2816-7155
ISBN 978-0-660-79454-9
Catalogue No. M183-2/9310E-PDF
https://doi.org/10.4095/pe2sqmjwm5

SUMMARY

As part of a study on lake talik formation, time-domain electromagnetic (TEM) soundings were conducted over First Landing Lake, and along a section from First Landing Lake to Second Landing Lake in the vicinity of Rankin Inlet, Nunavut. Second Landing Lake exhibits an electrical conductivity structure consistent with frozen and unfrozen ground, and is interpreted to support a talik to at least 100 m depth. First Landing Lake exhibits a more complicated electrical conductivity structure including high conductivity anomalies that may be associated with sublacustrine saline permafrost. The presence of a talik beneath First Landing Lake and the potential groundwater connectivity between the two lakes are challenging to interpret.

TABLE OF CONTENTS

INTRODUCTION

This Open File reports on time-domain electromagnetic (TEM) data collected over First Landing Lake and Second Landing Lake in the vicinity of Rankin Inlet, Nunavut. The TEM surveys were conducted with the objective of characterizing permafrost conditions as part of a larger study on lake taliks (LeBlanc et al., 2022; Sladen et al., 2024). For the Rankin Inlet region, sublacustrine permafrost and frozen ground are expected for water depths less than 1.1 m for which the duration of ice-substrate contact is long enough to sustain subzero mean annual temperature (LeBlanc et al., 2024). In contrast, taliks (unfrozen ground) are expected beneath deeper water. Talik depth will depend on the size and morphology of the lake, with the largest and deepest lakes supporting open or through taliks that penetrate permafrost completely and connect to the subpermafrost groundwater system.

Geophysical methods that are sensitive to electrical conductivity, such as TEM surveys, can provide non-invasive information on permafrost and groundwater conditions due to the strong dependence of electrical conductivity on the phase change of water to ice (e.g., Creighton et al., 2018). In general, frozen water and/or frozen substrate (permafrost) will have lower electrical conductivity than unfrozen water and/or unfrozen substrate (talik). Geophysical surveys collected over lake ice may be used to detect the presence of lake taliks, to distinguish between open and closed taliks, and to estimate talik depth.

STUDY AREA

The Hamlet of Rankin Inlet is located on the western coast of Hudson Bay in the Kivalliq Region of Nunavut, Canada (Figure 1). Rankin Inlet is within the continuous permafrost zone where 90–100% of the land area is underlain by permafrost (Heginbottom et al., 1995). Mean annual ground temperature at the top of permafrost varies from −9.5 to −5.5°C and active layer thickness ranges from 60 to 160 cm (LeBlanc and Oldenborger, 2021). The base of permafrost is variable at several hundred meters depth and is influenced by lake proximity (Golder Associates Ltd., 2021).

First Landing Lake and Second Landing Lake are located approximately 7 km northwest of the Hamlet of Rankin Inlet. First Landing Lake has an approximate volume of 4.2×10^6 m^3 with a maximum depth of 17.6 m (Budkewitsch et al., 2011). Second Landing Lake has a measured depth of 6.7 m (Oldenborger, 2024). Bedrock beneath the lakes is largely volcanic with sedimentary rocks crossing the centre of the lakes in the east-west direction (Golder Associates Ltd., 2021). The surrounding surficial geology is marine, glacial, and glaciofluvial with variable thickness, and some bedrock cliffs along the lake shores (McMartin, 2002). Both First Landing Lake and Second

Landing Lake are large enough and deep enough to support talik formation and potentially open taliks (LeBlanc et al., 2024). However, both lakes exhibit shallow terraces extending up to several hundred meters from the shorelines which may influence talik formation (Figure 1).

METHODS

Ice- and ground-based TEM data were collected from April 21–24, 2024 along a section over First Landing Lake and along a section from First Landing Lake to Second Lading Lake. The study area and sounding locations are shown in Figure 1. The sections were chosen to investigate the transition from deep water to a shallow terrace on the northern shore of First Landing Lake, and to investigate the offshore-onshore-offshore transition and possible hydrogeologic connectivity between First Landing Lake and Second Landing Lake.

Data Acquisition

TEM surveys involve the measurement of the transient magnetic field strength resulting from rapid turn-off of current in a transmitter loop. Data were collected with a digital 20-gate ProTEM-D receiver, a TEM47 transmitter, and a high-frequency receiver coil (31.4 m^2) manufactured by Geonics Ltd. In all cases, the transmitter utilized a 40 m × 40 m single-coil square loop of AWG 12 stranded copper wire with a measured resistance of 0.9 Ω at 16°C. Transmitter current was held at 3.0 A for all soundings. All soundings were acquired in an offset- loop configuration to mitigate induced polarization effects associated with the strong primary field at the loop centre (Geonics Ltd., 2011). Soundings were acquired at base frequencies of 285 Hz, 75 Hz, and 30 Hz. Schematic survey layout and an example field site are illustrated in Figure 2. There is significant overlap in the measurement intervals and gate times for the base frequencies used, but the multiple acquisitions allow for redundancy checks, and for flexible data selection and processing. Data were collected as three separate successive records per base frequency and each record was stacked for integration times of 8 s (285 Hz), 15 s (75 Hz), and 30 s (30 Hz). Gain was set variably to keep ambient noise below ±5 nV/m^2 in the last five time gates at any base frequency, and to avoid any early-time signal saturation (Geonics Ltd., 2011). Ambient noise records (data acquired in the absence of a transmitter signal) were collected at every site for each base frequency using the same stacking and gain parameters as the data.

Additional TEM soundings collected in April, 2023 were incorporated to extend coverage across the lakes (Figure 1). These additional soundings were collected using a central loop configuration with a 100 m × 100 m single-coil square loop and both TEM47 and TEM57 transmitters (Oldenborger, 2024). Only the TEM47 data from 2023 are utilized herein.

Processing and Inversion

For each base frequency, the induced receiver coil voltage was calculated as the gate-by-gate mean signed voltage for each of the three records. The corresponding noise level at each time gate was calculated as the maximum of the absolute ambient induced voltage and the standard deviation of the three stacked voltage records, plus a constant value 0.01 mV representative of instrument precision. Ambient noise was observed to be essentially random, but the data are typically less repeatable at later times and for lower base frequency.

The mean voltage measurements and noise for each base frequency were adjusted for nonlinear gain (Geonics Ltd., 2011) and normalized by transmitter area and current. Normalization is equivalent to transformation of the receiver coil voltage (mV/Am^2) to the time rate of change of the magnetic field (T/s). Following normalization, data were selected and combined to form a single composite sounding. Composite soundings were generally constructed using selected time gates with noise levels less than 2–3% from one or two base frequencies (285 Hz and 30 Hz for example) chosen without overlap to maximize the duration of low-noise measurements. Composite decays curves were transformed to late-time apparent resistivity (Spies and Eggers, 1986) which can be useful for comparing soundings and identifying data characteristics. Construction of an example composite sounding is illustrated in Figure 3 for Site 2401.

The composite TEM soundings were inverted individually for electrical conductivity using EM1DTM (Farquharson and Oldenburg, 1993). EM1DTM is a least-squares 1D inversion algorithm that operates on a multi-layer parameterization. The data were fit using both L^2 (least-squares or "smooth") and L^1 (minimum length or "blocky") constraints on the model structure (Farquharson and Oldenburg, 1998). The model was over-parameterized with 30 layers increasing in thickness by a factor of 1.1, from 1 m at the surface to approximately 11 m at 100 m depth. The initial and reference models were homogeneous with electrical conductivity equal to that of the best-fit halfspace for the data. Model reliability was assessed by considering the data noise, the data misfit, and the model stability as quantified by the depth of investigation index (DOI, Oldenburg and Li 1999). To further aid interpretation, the TEM soundings were also inverted using a four-layer parametric inversion (Appendix A).

Both inversion algorithms incorporate variable noise weighting and attempt to fit the data to a level commensurate with the noise according to the discrepancy principle. In practice, convergence to prediction errors in excess of the data noise is generally acceptable considering that data from different base frequencies are not always consistent, and that noise levels are likely underestimated, especially for high frequencies and early times for which the data are highly repeatable but subject to systematic errors such as geometry errors, or violation of the 1D assumption.

RESULTS

The recovered electrical conductivity models for Site 2401 are illustrated in Figures 4 and 5. The L^2 model results in the best data fit and is characterized by a conductive layer starting at approximately 18 m depth and a resistive layer starting at approximately 55 m depth. The L^1 model is similar to the L^2 model but is more resistive at depth. An additional L^{1*} model results in reasonable data fit but exhibits very high conductivity (> 10^6 mS/m) below 40 m depth. Similar models, including the high conductivity excursion, are obtained for the four-layer inversion (Figure 5). Prediction errors for the four-layer inversions are consistently greater than those for the multi-layer inversions due to the limited model freedom.

Differences between the recovered models provide some information on model uncertainty. An additional measure of model uncertainty is given by the DOI illustrated for Site 2401 in Figure 6. For this site, it is evident that the model uncertainty increases rapidly beyond 50 m depth, which is near the point of departure for the models of Figures 4 and 5 and the depth of the high conductivity excursion.

The occurrence of very high conductivity is prevalent in the Rankin Inlet TEM inversions and tends to be exacerbated by conductive best-fit initial conditions. Models with conductivity greater than 10^5 mS/m are considered unrealistic and not accepted as final solutions (e.g., Palacky, 1998). In some cases, these models can be avoided by choice of base frequency, editing of high-noise data, or specifying more resistive initial conditions. In other cases, the high- conductivity artefacts are persistent, but can typically be tempered by removal of late-time data.

In particular, rapid late-time upturns in apparent resistivity are an indication of 3D effects in the data caused by off-loop conductive structure (Newman et al., 1987). When data are removed beyond any severe upturn in the apparent resistivity curve, models can be well-fit and interpreted approximately to the depth of the offending 3D structure (Newman et al., 1987). This procedure is illustrated for Site 2404 in Figure 7 for which a significant upturn in apparent resistivity is observed at approximately 0.1 ms. Using the full composite sounding curve results in poor data fit, strong shallow model oscillations, and runaway conductivity at 30–40 m depth. If the data are limited to gates earlier than 0.1 ms, data fit is greatly improved, the oscillations are reduced, and the top of a strong (but not unreasonable) conductor is well-resolved at 32 m depth beyond which the model becomes uncertain.

Models obtained from the 1D inversions were horizontally interpolated to create pseudo-2D sections for each model type. Results are shown in Figures 8–10 north from the centre of First Landing Lake to the shore, and in Figures 11–13 east from Second to First Landing Lake. The pseudo-2D sections are largely consistent across model type with the L^2 models providing the most complex model structure, and the four-layer models providing the most basic model structure. The levels of data fit vary considerably with Site 2416 having notably poor fit but similar structure to adjacent soundings (e.g., Figure 12).

For Site 2401 on First Landing Lake, water depth is approximately 6 m (Budkewitsch et al., 2011), ice thickness is approximately 1.7 m, and in-situ water conductivity is approximately 20 mS/m (Oldenborger, 2024; Oldenborger, 2025). The recovered electrical conductivity is 14– 18 mS/m to a depth of 16 m (Figure 9) suggesting that there is no significant conductivity contrast between the lake water and (unfrozen) substrate. Below the lake bottom, a shallow conductor (~100–500 mS/m) is evident that increases in depth from very near the surface at the shoreline (Site 2405) to 20–30 m depth offshore (Sites 2401 and 2312). There is also some evidence for deeper, stronger conductors (10^3–10^4 mS/m) at Sites 2403–2405 below the lake terrace, and at Site 2312 (Figure 9). However, these conductors are near or below the limit of the DOI and are associated with increased data misfit.

For Second Landing Lake there does appear to be a weak contrast in electrical conductivity associated with the lake bottom at Sites 2315 and 2316 (Figure 12). However, the higher conductivity surface layer appears to thicken under the lake terrace (Site 2319) and extends onshore (Site 2418). There is no shallow conductor apparent below the bottom of Second Landing Lake. Instead, the recovered models suggest a general increase in conductivity with depth below the lake bottom (Sites 2315 and 2316). The eastern shore of Second Landing Lake is characterized by resistive ground (Sites 2416–2418), but the western shore of First Landing Lake exhibits a high conductivity anomaly (Sites 2411–2413) similar to that on the northern shore (Figure 9). The large loop soundings over Second Landing Lake (Sites 2315–2317) do not exhibit a deep runaway conductor as observed over First Landing Lake (Site 2312).

DISCUSSION

The pseudo-2D electrical conductivity sections suggest differing and complicated permafrost conditions for First and Second Landing Lake. The section for Second Landing Lake (e.g., Figure 13) is interpreted as representing a talik (unfrozen ground) to at least 100 m depth that is more conductive than onshore permafrost. The increase in conductivity at depth below Second

Landing Lake (Sites 2415 and 2416) may result from a transition from fresh surface water to deeper saline water (e.g., Golder Associates Ltd., 2021). The talik and conductive ground are more pronounced under the deeper water of the eastern side of Second Landing Lake (Site 2315) with a transition to resistive frozen ground under the western terrace (Site 2317). The eastern onshore soundings (Sites 2416–2418) exhibit a transition to more conductive ground at depths greater than 65–75 m, suggesting that the talik may extend under the eastern shore of Second Landing Lake. The conductivity structure of Second Landing Lake appears mostly consistent with the simple conceptual model of conductive unfrozen ground (talik) and resistive frozen ground (onshore permafrost). The nature of the moderately conductive surface layer is unknown but may be related to unconsolidated sediments overlying bedrock.

In contrast, First Landing Lake (e.g., Figures 10 and 13) exhibits a shallow conductive layer near 20 m depth that is persistent across all soundings and gets shallower under the lake terraces on both shores. Off the terraces, the conductive layer is underlain by resistive ground suggestive of frozen ground or fresh water (Sites 2401, 2402, and Sites 2408–2410 with the exception of Site 2312 below the DOI). Under the terraces and under the western shore of First Landing Lake, the shallow conductive layer is underlain by even stronger conductive anomalies (Sites 2403–2405 and Sites 2411–2413). First Landing Lake is deeper than its counterpart, such that a talik on Second Landing Lake would imply the same for First Landing Lake, but the geophysical signatures are not the same. Variations in bedrock or surficial geology are not likely explanations for the observed high conductivity. However, saline permafrost has been observed in other studies in the region and could be responsible for the electrical conductivity structures observed under First Landing Lake.

Saline permafrost is associated with high electrical conductivity due to increased pore water salinity, depressed freezing point, and increased unfrozen water content. Saline permafrost complicates the simple conceptual model for taliks and may result in an off-loop response for TEM soundings identified in the TEM data as severe upturns in apparent resistivity (e.g., Figure 7, Site 2404). Although attempts have been made to remove affected late-time data, influence of off-loop high conductivity may remain, and the manifestation of 3D effects on 1D TEM models can be severe and counter-intuitive. High conductivity layers, runaway conductivity, and complicated model structure such as very thin layers or strong conductive- resistive oscillations are documented artefacts of 3D effects in 1D TEM inversion (Newman et al., 1987; Yang and Oldenburg, 2012). In particular, existence of saline permafrost below the northern terrace of First Landing Lake has been interpreted from other geophysical data (Oldenborger, 2025). Shallow high conductivity saline permafrost isolated below the lake terraces of First Landing Lake could result in 3D effects such as a shallow conductive artefact persistent across the lake, although this hypothesis remains to be tested with synthetic modelling.

Induced Polarization (IP) has also been identified as a potential source of complicated TEM soundings and models (Lorentzen et al., 2024). Even with an offset-loop configuration, IP effects may be present in permafrost terrain and will confound interpretation if not explicitly accounted for. IP effects are most influenced by the near surface and typically result in negative transients, or sign reversals of the TEM decay at late times (Smith and West, 1989; Macnae, 2016). Although late-time sign reversals are observed in the Rankin Inlet TEM data, the negative data are never of a magnitude in excess of the ambient noise, and high conductivity layers or runaway conductivity are not documented artefacts of IP contamination of TEM data. Early-time sign reversals are observed for the Rankin Inlet TEM data (Figure 7) but are associated with the offset geometry and sign reversal of the induced magnetic field resulting from slow current diffusion over conductive ground (Ward and Hohmann, 1988). For sufficiently resistive ground, current diffusion is fast enough that no sign reversal is observed (Figure 3). In this respect, off- loop saline permafrost may have a significant effect by influencing the negative-positive crossover which is difficult to model precisely.

CONCLUSION

TEM soundings were conducted over First Landing Lake and along a section from First Landing Lake to Second Landing Lake in the vicinity of Rankin Inlet, Nunavut. Survey results show variations in electrical conductivity interpreted to result from both frozen and unfrozen ground, and potential sublacustrine saline permafrost. Second Landing Lake exhibits an electrical conductivity structure consistent with the conceptual model for frozen and unfrozen ground and is interpreted to support a talik to 100 m depth or more. The talik may extend under the eastern shore of Second Landing Lake. In contrast, First landing Lake exhibits a complicated electrical conductivity structure that may be a result of saline permafrost and associated 3D artefacts in the 1D TEM inversions. The presence of a talik beneath First Landing Lake and the potential groundwater connectivity between the two lakes are challenging to interpret.

ACKNOWLEDGEMENTS

Part of the Natural Resources Canada GEM-GeoNorth Program. Data collected with assistance from C. Duchesne. Ice survey and lake depth data provided by W. Sladen. Internal review by B. Dietiker.

REFERENCES

Budkewitsch, P., Prévost, C., Pavlic, G., Pregitzer, M., 2011. Description of water depth survey datasets from Rankin Inlet, Nunavut. Geological Survey of Canada, Open File 6751. https://doi.org/10.4095/288667

Creighton, A.L., Parsekian, A.D., Angelopoulos, M., Jones, B.M., Bondurant, A., Engram, M., Lenz, J., Overduin, P.P., Grosse, G., Babcock, E., Arp, C.D., 2018. Transient electromagnetic surveys for the determination of talik depth and geometry beneath thermokarst lakes. Journal of Geophysical Research: Solid Earth 123, 9310–9323. https://doi.org/10.1029/2018JB016121

Farquharson, C.G., Oldenburg, D.W., 1993. Inversion of time-domain electromagnetic data for a horizontally layered Earth. Geophysical Journal International 114, 433–442. https://doi.org/10.1111/j.1365-246X.1993.tb06977.x

Farquharson, C.G., Oldenburg, D.W., 1998. Non-linear inversion using general measures of data misfit and model structure. Geophysical Journal International 134, 213–227. https://doi.org/10.1046/j.1365-246x.1998.00555.x

Geonics Ltd., 2011. PROTEM 47D Operating Manual for 20/30 Gate Model.

Golder Associates Ltd., 2021. Summary of Hydrogeology Existing Conditions, Meliadine Extension. Report No. 20136436-855-R-ExistingConditionsReport-Rev3, Agnico Eagle Mines Limited.

Heginbottom, J.A., Dubreuil, M.H., Harker, P.T., 1995. Canada, Permafrost. National Atlas of Canada, 5th ed., Plate 2.1, MCR 4177.

Lagarias, J.C., Reeds, J.A., Wright, M.H., Wright, P.E., 1998. Convergence properties of the Nelder-Mead simplex method in low dimensions. SIAM Journal of Optimization 9, 112–147. https://doi.org/10.1137/S1052623496303470

LeBlanc, A.-M., Chartrand, J., Smith, S.L., 2022. Regional assessment of the presence of taliks below Arctic lakes, Nunavut. Geological Survey of Canada, Scientific Presentation 138. https://doi.org/10.4095/330205

LeBlanc, A-M, Sladen, W.E, Faucher, B., 2024. Lake-bottom temperature on shallow and deep terraces for sublacustrine open talik assessment near Rankin Inlet, Nunavut, Canada. International Conference on Permafrost, 378–379.

Lorentzen, T.H., Kass, M.A., Scheer, J., Tomaškovičová, S., Christiansen, A.V., Maury, P.K., Ingeman-Nielsen, T., 2024. Exploring the challenges of interpreting near-surface towed TEM data on saline permafrost. Geophysics 1–51. https://doi.org/10.1190/geo2023-0221.1

Macnae, J., 2016. Quantifying airborne induced polarization effects in helicopter time domain electromagnetics. Journal of Applied Geophysics 135, 495–502.

https://doi.org/10.1016/j.jappgeo.2015.10.016
McMartin, I. 2002. Surficial geology, Rankin Inlet, Nunavut. Geological Survey of Canada, Open File 4116. https://doi.org/10.4095/299616
Newman, G.A., Anderson, W.L., Hohmann, G.W., 1987. Interpretation of transient electromagnetic soundings over three-dimensional structures for the central-loop configuration. Geophysical Journal International 89, 889–914. https://doi.org/10.1111/j.1365-246X.1987.tb05200.x
Oldenborger, G.A., 2024. Time-domain electromagnetic soundings for talik investigations, Rankin Inlet, Nunavut. Geological Survey of Canada, Open File 9170. https://doi.org/10.4095/p60hysa40q
Oldenborger, G.A., 2025. Electromagnetic mapping of sublacustrine saline permafrost, Rankin Inlet, Nunavut, Nunavut. Geological Survey of Canada, Open File 9289. https://doi.org/10.4095/pqunx9q1bk
Oldenburg, D., Li, Y., 1999. Estimating depth of investigation in dc resistivity and IP surveys. Geophysics 64, 403–416. https://doi.org/10.1190/1.1444545
Palacky, G.J., 1988. Resistivity characteristics of geologic targets, in: Nabighian, M.N. (Ed.), Electromagnetic Methods in Applied Geophysics, Investigations in Geophysics. Society of Exploration Geophysicists, 53–129.
Sladen, W.E., LeBlanc, A.-M., Chartrand, J., van der Sanden, J., 2024. Using RADARSAT constellation mission imagery to support talik mapping, Rankin Inlet, Nunavut, Canada. Proceedings of the International Conference on Permafrost, 390–397.
Smith, R.S., West, G.F., 1989. Field examples of negative coincident-loop transient electromagnetic responses modeled with polarizable half-planes. Geophysics 54, 1491–1498. https://doi.org/10.1190/1.1442613
Spies, B.R., Eggers, D.E., 1986. The use and misuse of apparent resistivity in electromagnetic methods. Geophysics 51, 1462–1471. https://doi.org/10.1190/1.1442194
Ward, S.H., Hohmann, G.W., 1988. Electromagnetic theory for geophysical applications, in: Nabighian, M.N. (Ed.), Electromagnetic Methods in Applied Geophysics, Investigations in Geophysics. Society of Exploration Geophysicists, 53–129.
Yang, D., Oldenburg, D.W., 2012. Three-dimensional inversion of airborne time-domain electromagnetic data with applications to a porphyry deposit. Geophysics 77, B23–B34. https://doi.org/10.1190/geo2011-0194.1

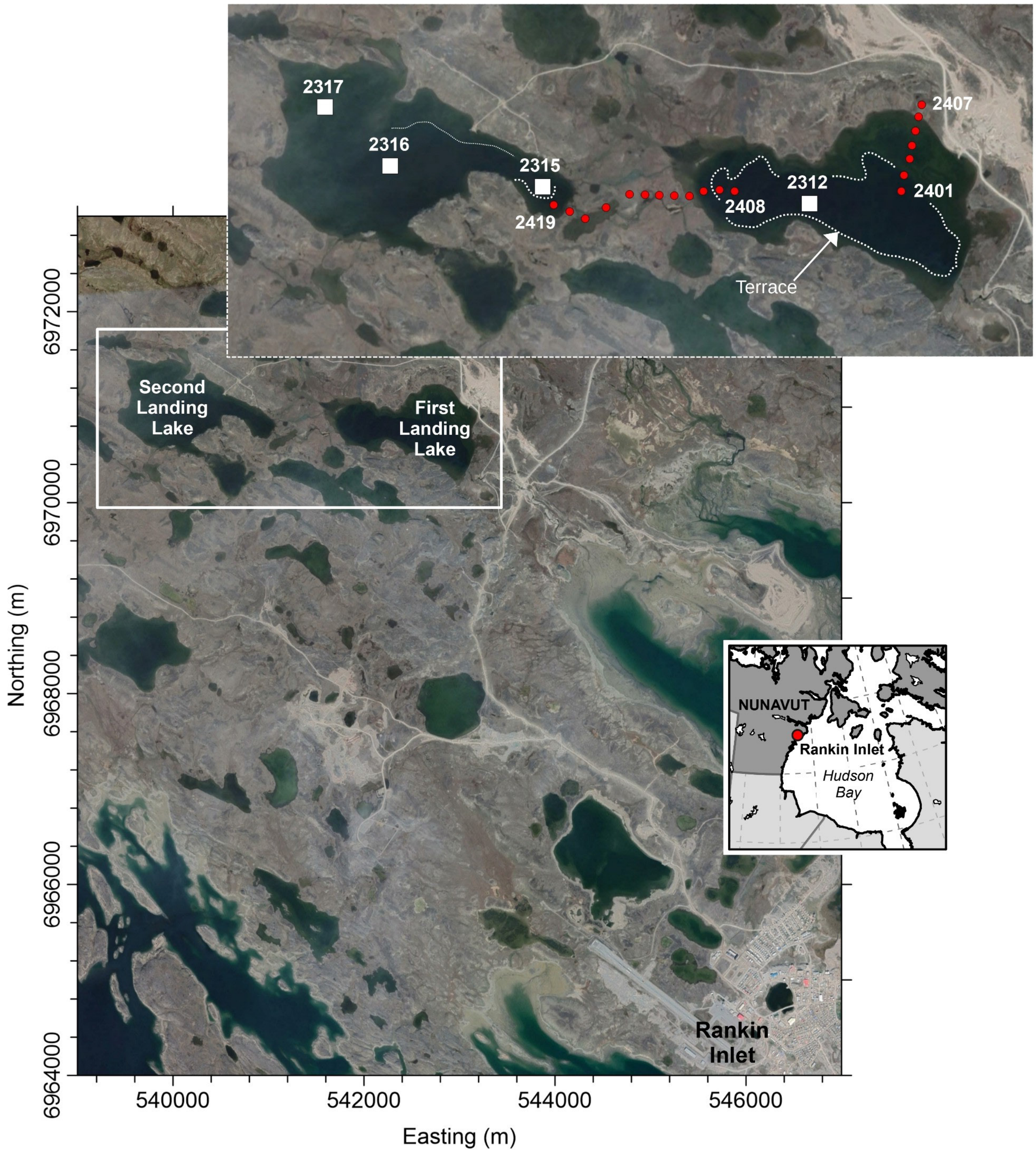

Figure 1. Study area near Rankin Inlet, Nunavut. Sounding locations across First Landing Lake and Second Landing Lake are shown as red circles. Additional soundings from Oldenborger (2024) are shown as white squares. Coordinates are Easting and Northing, WGS84 UTM Zone 15N. Background image: Google Earth, © 2023 Maxar Technologies, © 2023 TerraMetrics.

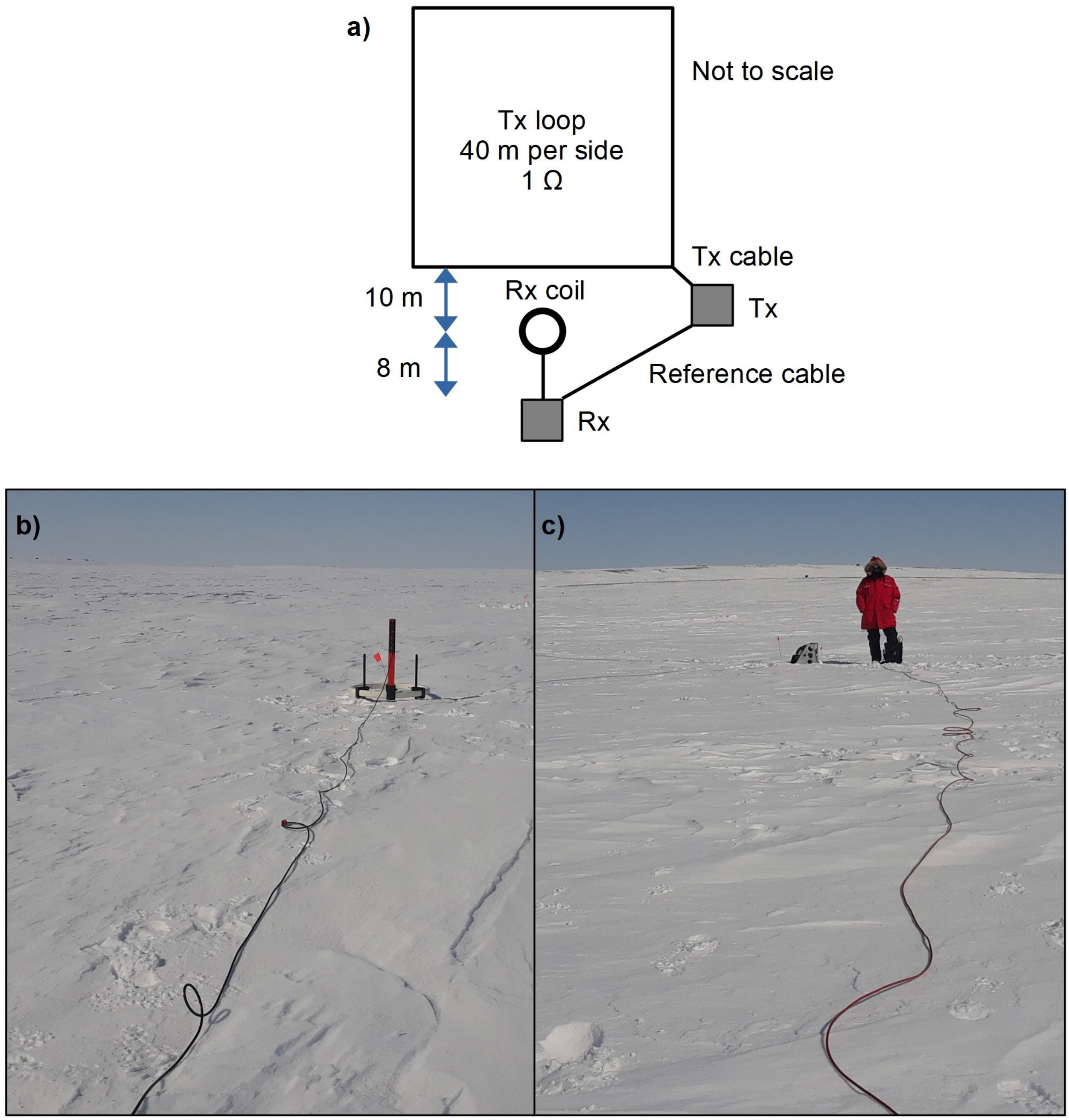

Figure 2. a) Schematic of TEM survey layout (not to scale). b) View looking south towards the receiver coil at Site 2403, First Landing Lake. c) View looking northeast towards the transmitter and operator at Site 2403, First Landing Lake. Photographs by G. Oldenborger.

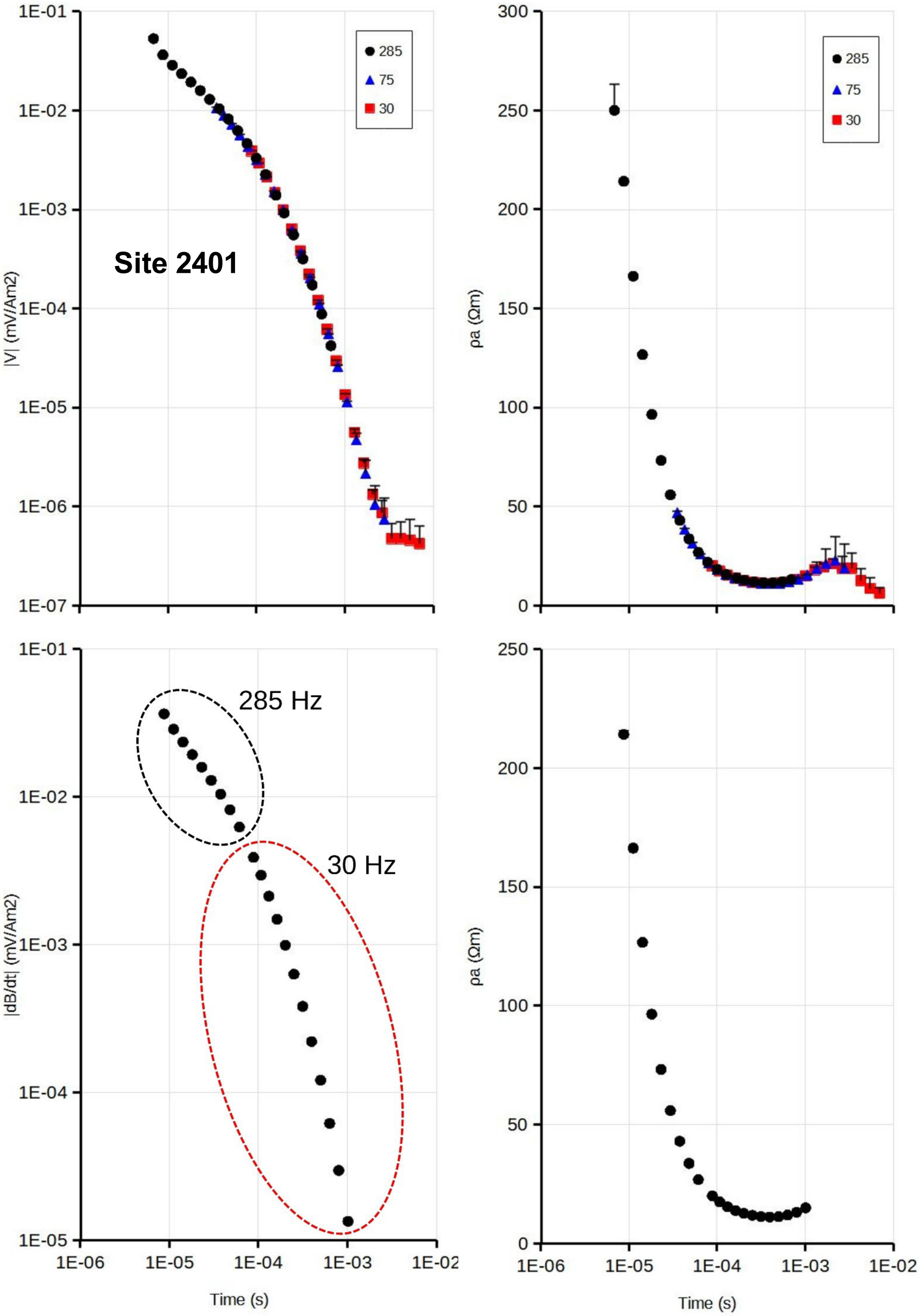

Figure 3. Construction of composite sounding and apparent resistivity curves for Site 2401. Top: normalized receiver voltage as a function of time (20 gates) for all three base frequencies (left) and the transformation to apparent resistivity (right). Bottom: composite decay curve constructed from gates 2–10 at 285 Hz and gates 1–12 at 30 Hz (left) and the transformation to apparent resistivity (right). Maximum measurement noise for the composite curve is 2.6% with minimum resolved voltage of approximately $1{\times}10^{-5}$ mV/Am^2 at 1 ms.

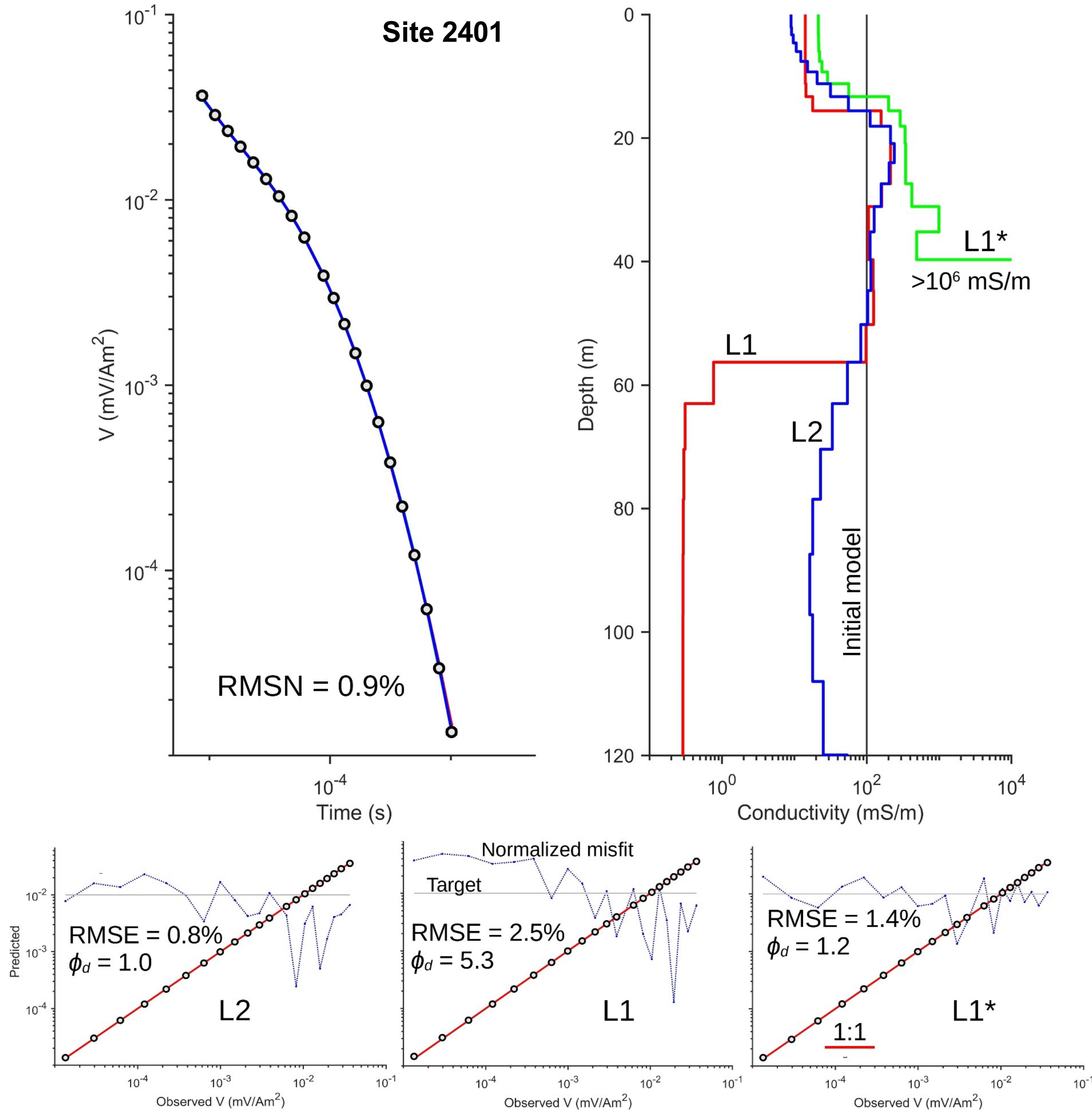

Figure 4. Multi-layer inversions for Site 2401. Top: composite sounding (left) and recovered multi-layer electrical conductivity models (right). Models shown are the L^2 model, the L^1 model, and an L^{1*} model obtained using a conductive initial model. Bottom: the predicted data are visually indistinguishable from the observed data. Root-mean-square error of the predicted data (RMSE) is comparable to root-mean-square noise (RMSN).

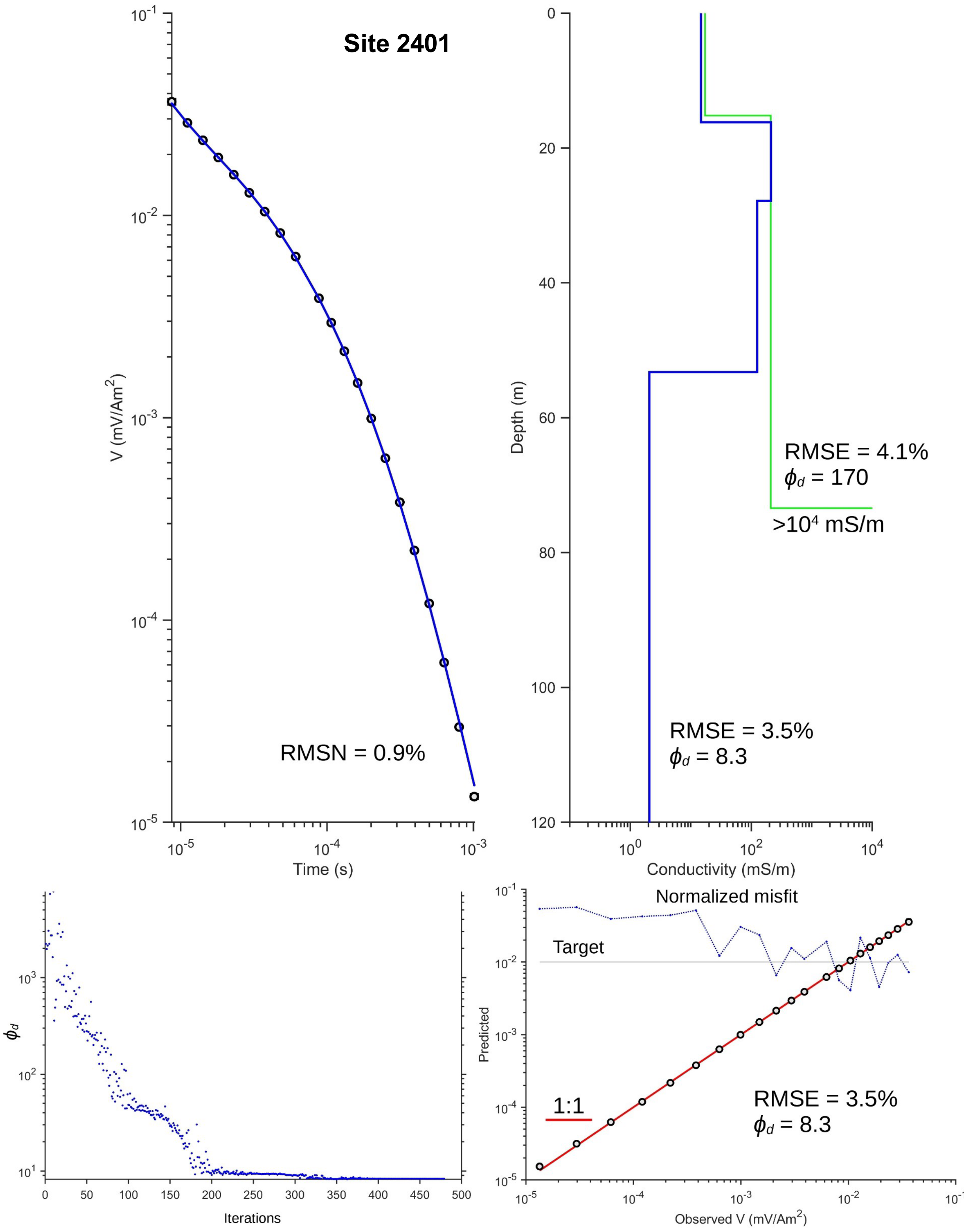

Figure 5. Four-layer inversions for Site 2401. Top: composite sounding (left) and recovered electrical conductivity models (right). Models shown are for solutions obtained from initial conditions given by the L^1 (blue) and L^{1*} (green) models in Figure 4.

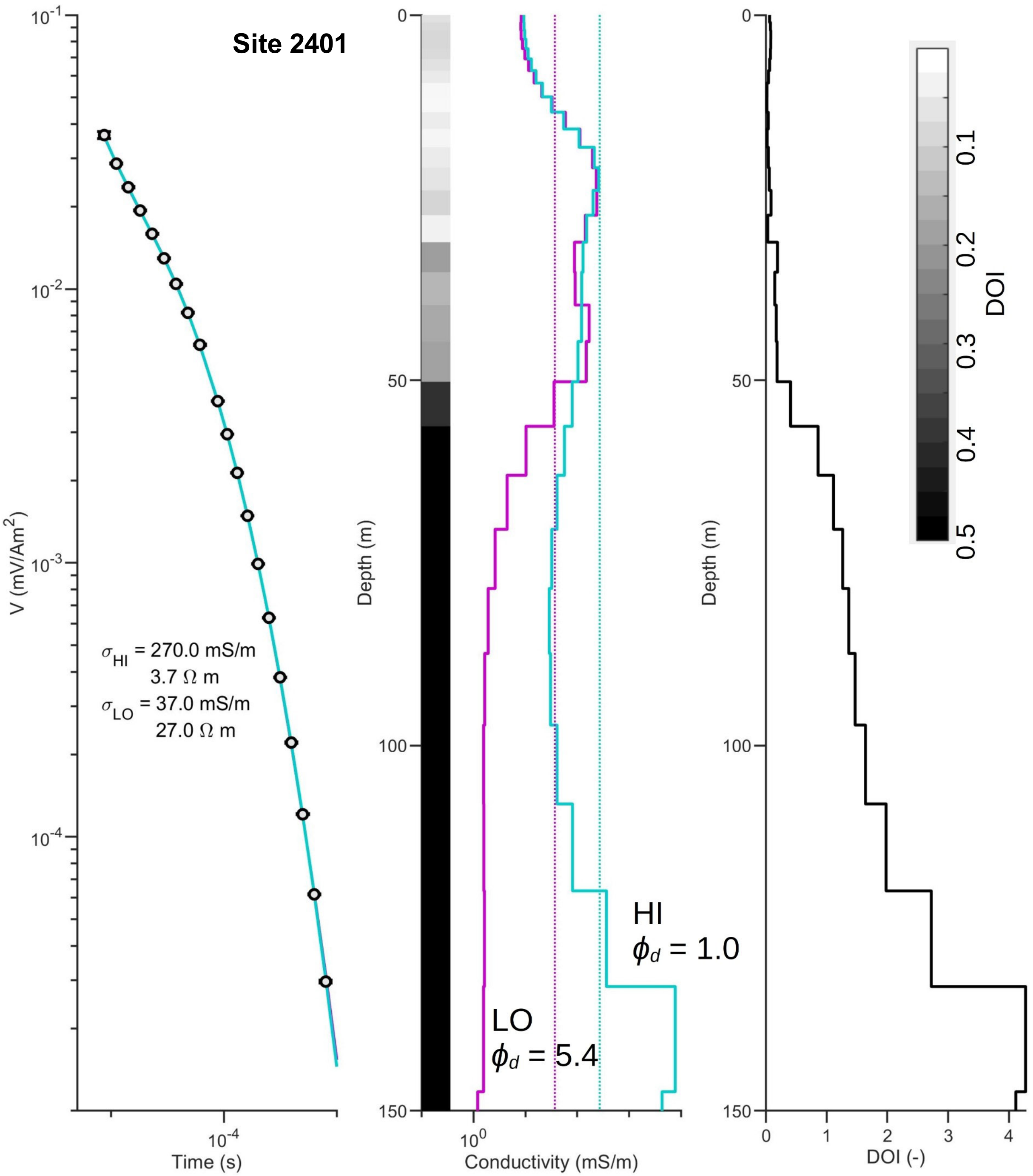

Figure 6. Depth of investigation index (DOI) for Site 2401 obtained through inversion using high- and low-sided reference models.

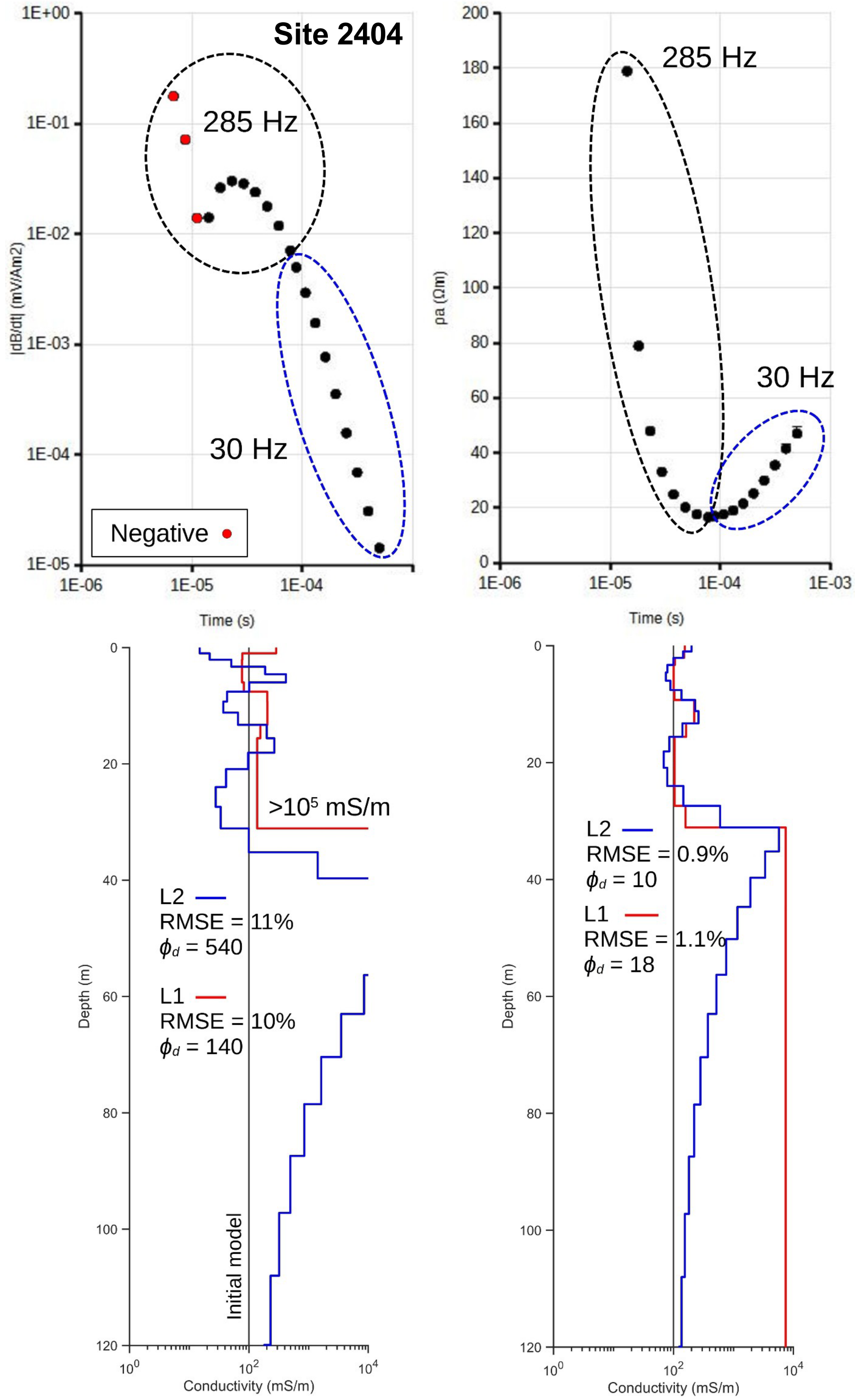

Figure 7. Site 2404. Top: composite sounding (left) and apparent resistivity curve (right) constructed from gates 1–11 at 285 Hz and gates 1–7 at 30 Hz. Bottom: recovered multi-layer electrical conductivity models for the entire composite sounding (left) and for 285 Hz only (right).

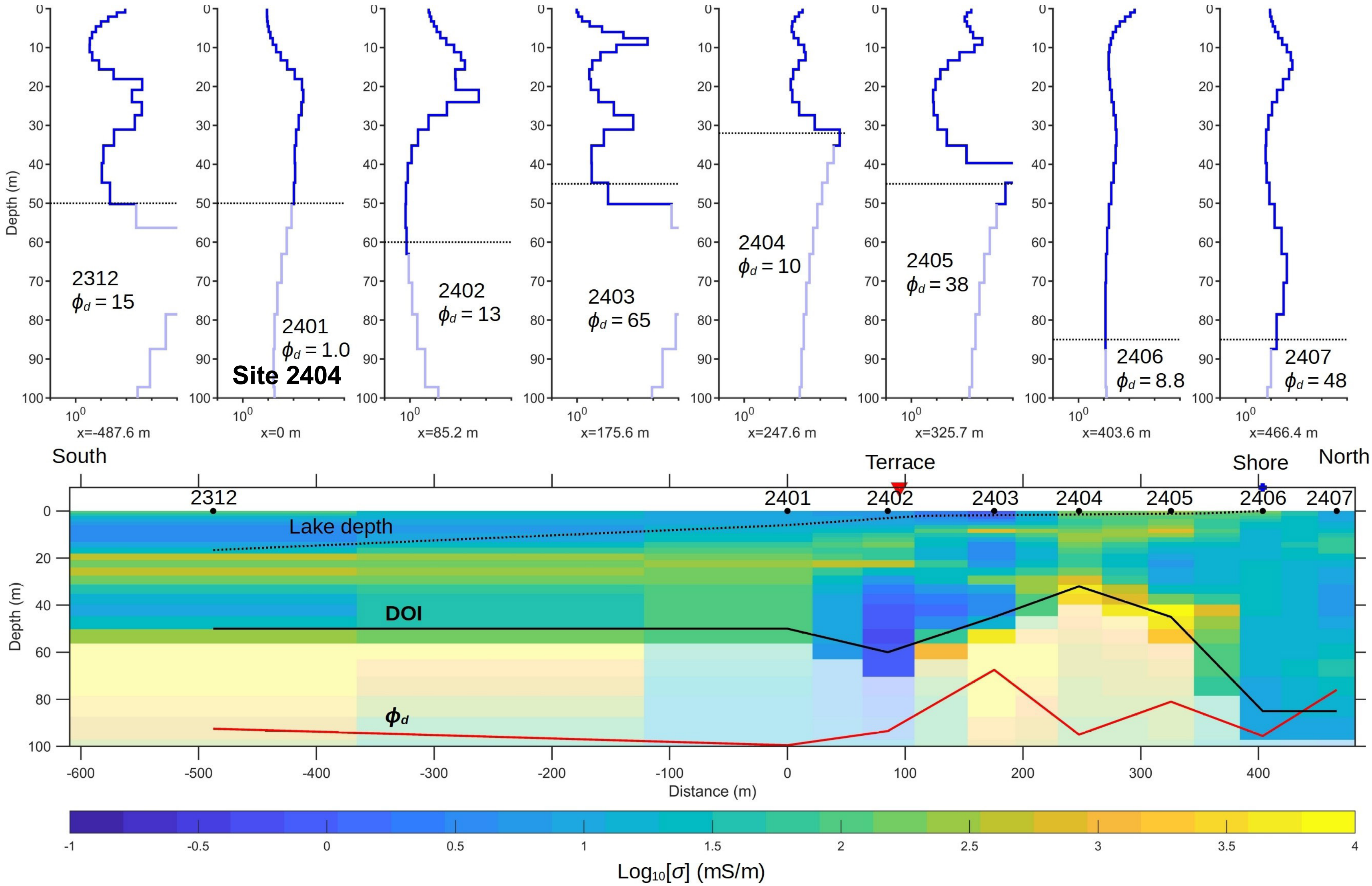

Figure 8. South-to-north conductivity section across First Landing Lake from the lake centre to the northern shore. Horizontally interpolated multi-layer 1D L^2 models. Vertical exaggeration 2:1.

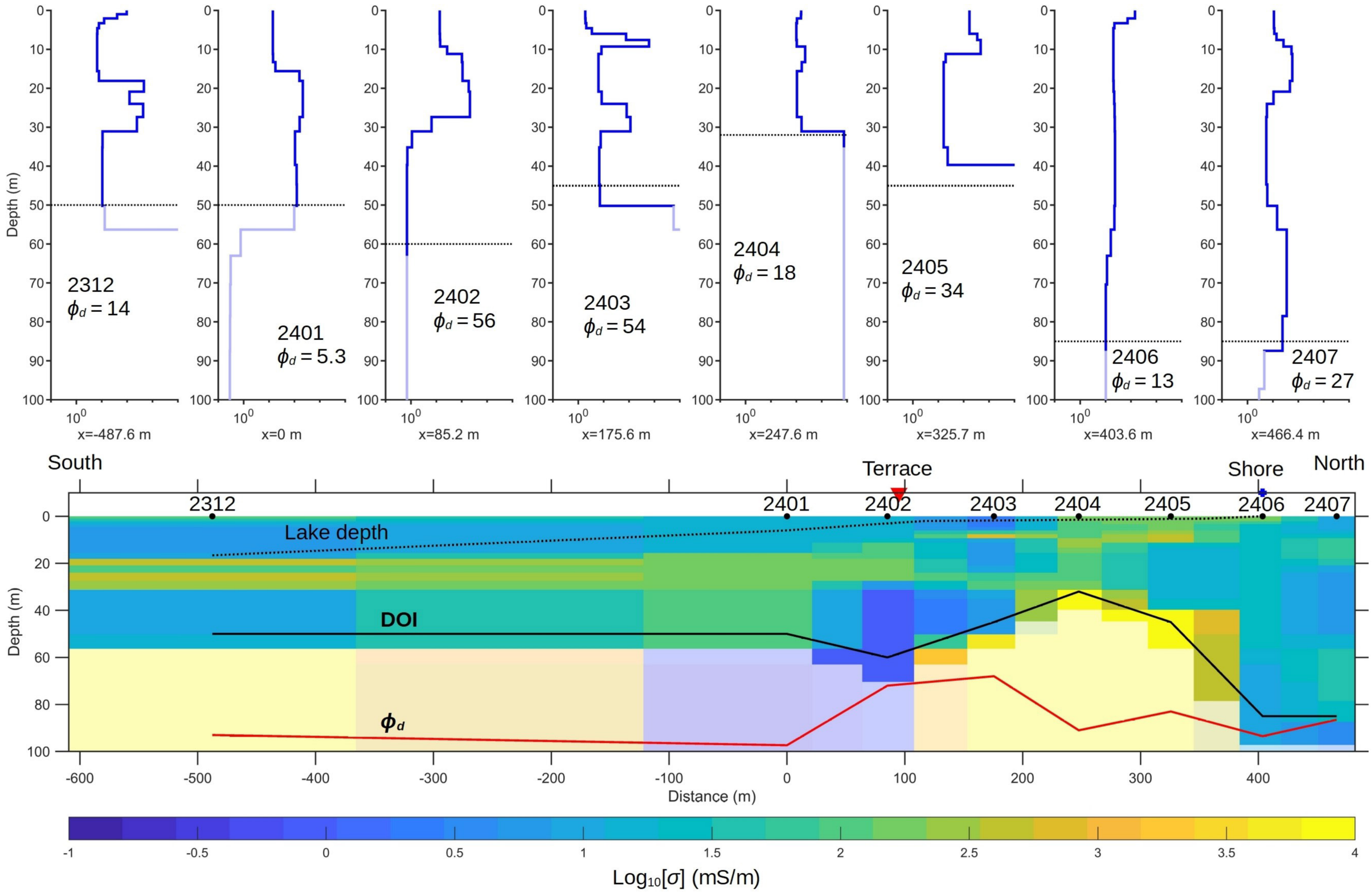

Figure 9. South-to-north conductivity section across First Landing Lake from the lake centre to the northern shore. Horizontally interpolated multi-layer 1D L^1 models. Vertical exaggeration 2:1.

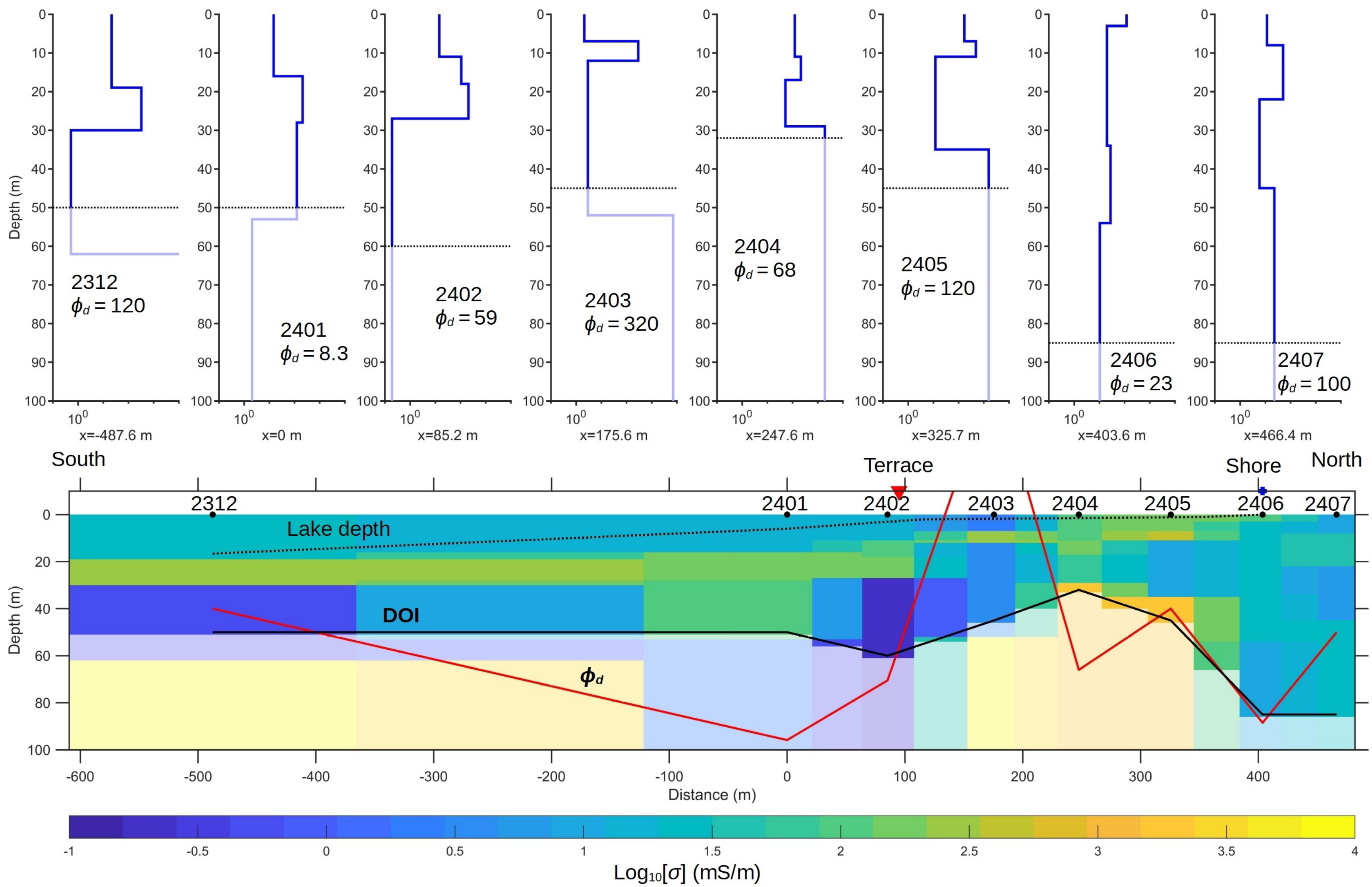

Figure 10. South-to-north conductivity section across First Landing Lake from the lake centre to the northern shore. Horizontally interpolated four-layer 1D models. Vertical exaggeration 2:1.

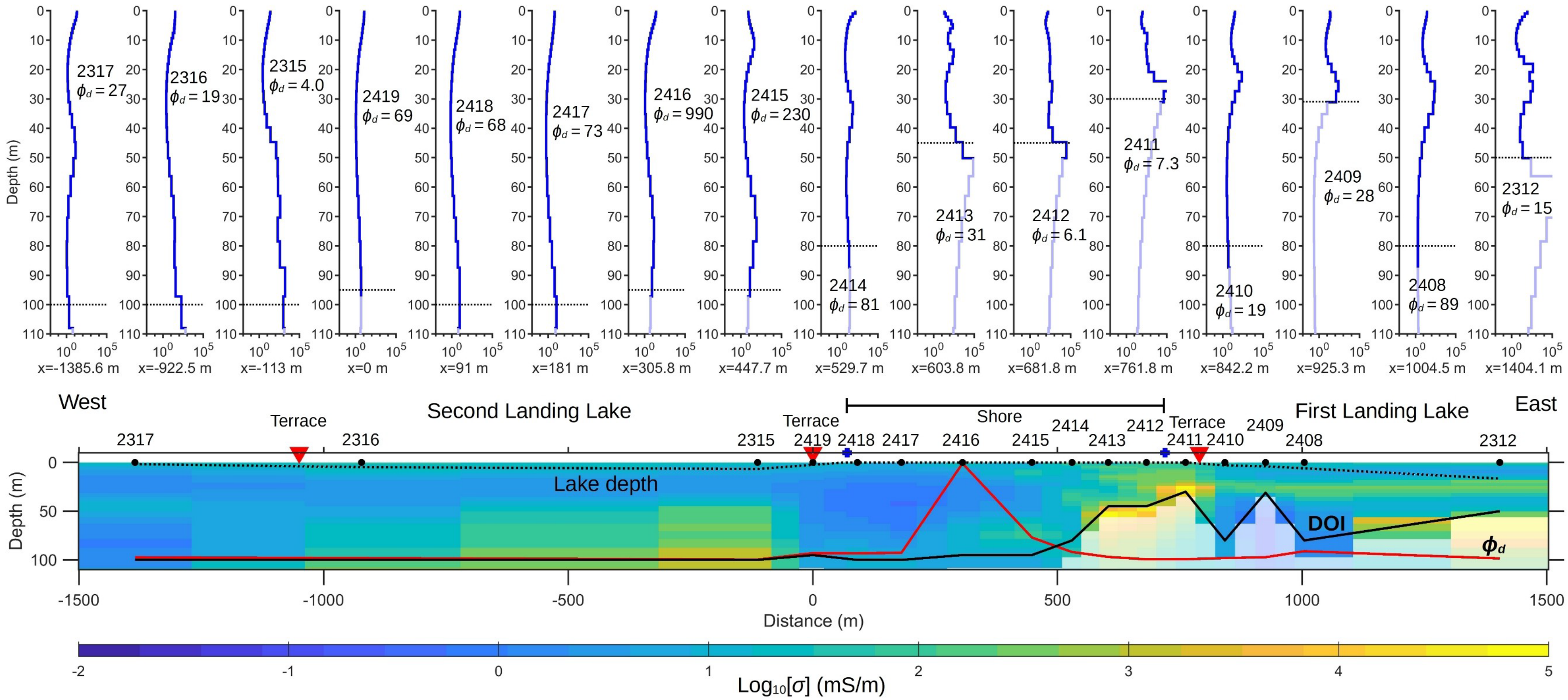

Figure 11. West-to-east conductivity section from Second to First Landing Lake. Horizontally interpolated multi-layer 1D L^2 models. Vertical exaggeration 2:1.

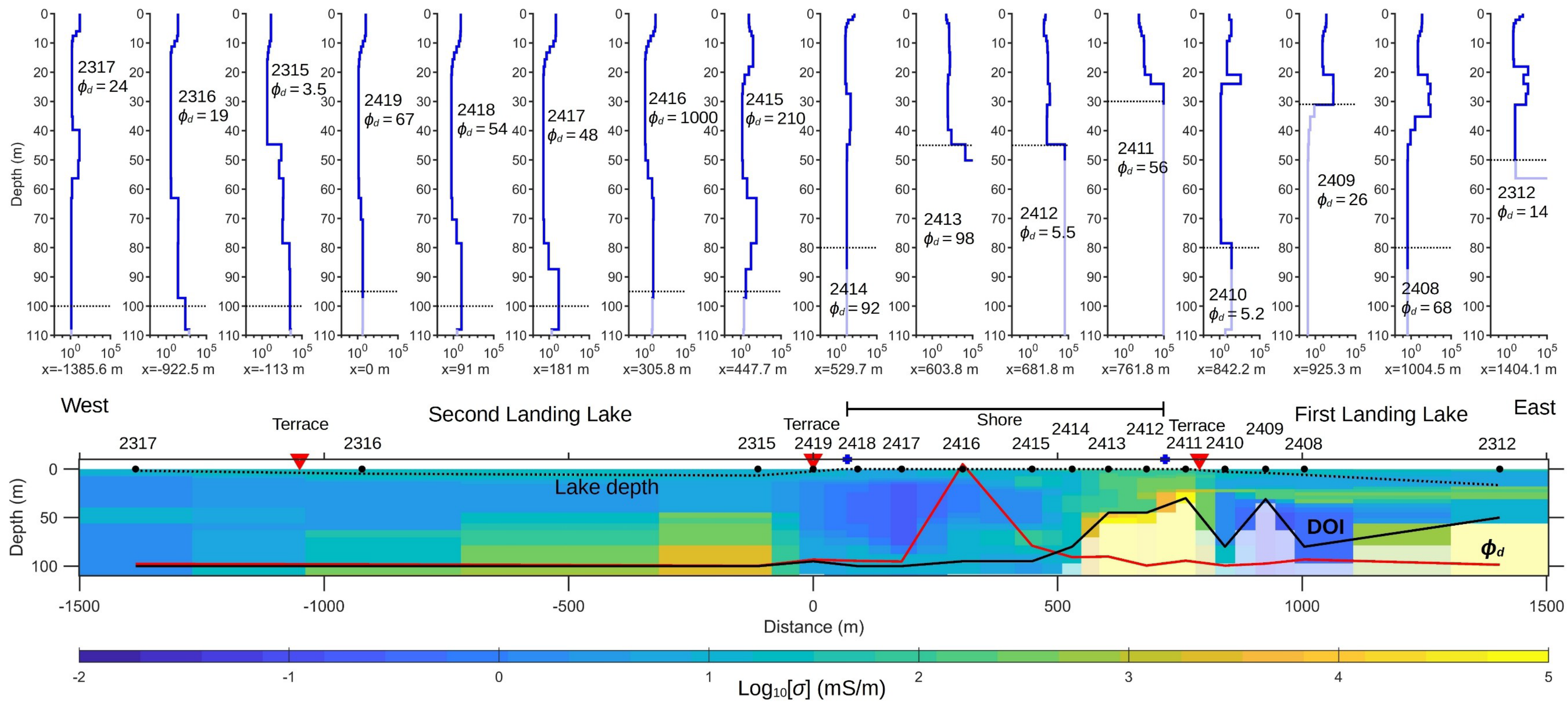

Figure 12. West-to-east conductivity section from Second to First Landing Lake. Horizontally interpolated multi-layer 1D L^1 models. Vertical exaggeration 2:1.

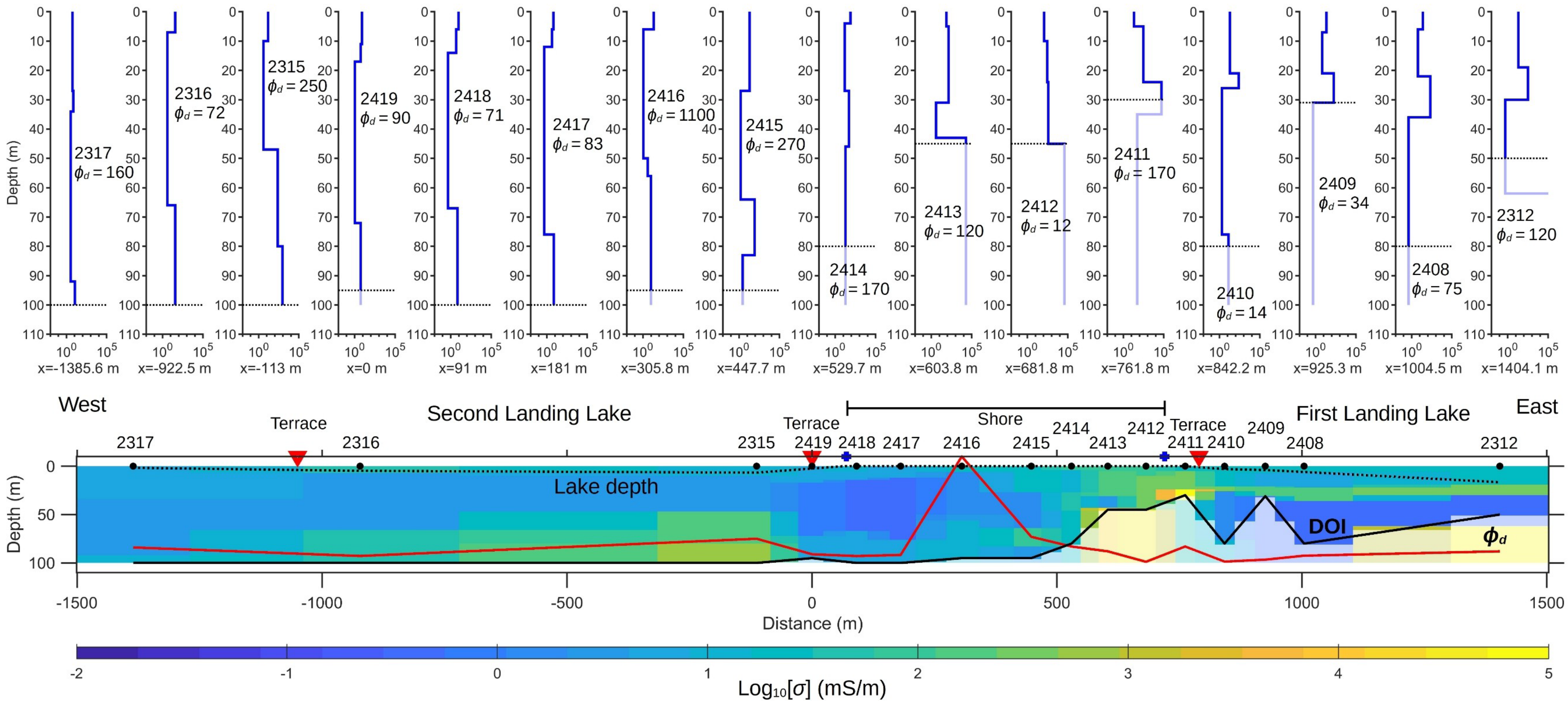

Figure 13. West-to-east conductivity section from Second to First Landing Lake. Horizontally interpolated four-layer 1D models. Vertical exaggeration 2:1.

APPENDIX A

For a time-domain electromagnetic survey, measurements consist of secondary magnetic field strength as a function of time, usually recorded as voltage induced in a receiver coil (e.g., Geonics, 2011). For the 20-gate ProTEM-D receiver, data consist of measured voltage over 20 logarithmically-spaced gates for a number of records at variable base frequency. Each base frequency is characterized by different transmitter turn-off times, different gate windows, and different length off-times. Records from multiple base frequencies can be combined into a composite decay curve to increase receiver bandwidth.

The data can be inverted to recover electrical conductivity by minimizing the least-squares prediction error subject to model constraints as described by objective functions for both the data and the model. The data objective function is formulated as

$$\psi_d = |\phi_d - 1|_2 \quad \text{where} \quad \phi_d = \frac{1}{N}\sum_{i=1}^{N}\left[\frac{d_i - f_i(m)}{e_i}\right]^2$$

where d_i is the receiver voltage for channel i, $f_i(m)$ is the simulated voltage as a function of the model m, e_i is the standard deviation of the ith datum, and N is the number of data ($N = 20$ for a single 20-gate ProTEM sounding). For normally distributed prediction errors, ϕ_d takes the form of the reduced chi-squared distribution with an expected value of unity. When ψ_d is minimized to zero, $\phi_d = 1$, and the prediction errors are commensurate with the standard deviation of the data in accordance with the discrepancy principle. In the case that ψ_d cannot be minimized to zero, the value of ϕ_d at convergence gives a measure of the sum-squared prediction error relative to the data error.

The model objective function is formulated as

$$\psi_m = \frac{1}{M}\sum_{j=1}^{M}\left(\alpha_j\left[\frac{m_j - m_j^r}{m_j^r}\right]^2 + \beta_j\left[\frac{d}{dz}\frac{\sigma_j}{\sigma_j^r}\right]^2 + b_{min}\left[\frac{\max\left(0, m^{min} - m_j\right)}{m_j^r}\right]^2 + b_{max}\left[\frac{\max\left(0, m_j - m^{max}\right)}{m_j^r}\right]^2\right)$$

where m^r is a reference model, m^{min} is a lower bound model, m^{max} is an upper bound model, and M is the number of model layers. The weight α_j controls the reference model regularization, and the weight β_j controls the smoothness regularization for the jth layer. The weights b_{min} and b_{max} control the barrier terms for the lower and upper model bounds m^{min} and m^{max}. The model m takes the form of a set of conductivity-thickness parameter pairs $m_j = [\sigma_j, L_j]$ or log-transformed conductivity-thickness parameter pairs $m_j = \ln[\sigma_j, L_j]$ where the thickness of the bottom layer is fixed and infinite. For the log-transformed model, the terms in the model objective function are *not* normalized by the reference model since the log transform is unitless and accounts for scaling without the need for normalization. Log transformation is used hereafter.

The total objective function $\psi = \psi_d + \psi_m$ is minimized using Nelder-Mead simplex optimization (Lagarias et al., 1998) with implicit model constraints given by ψ_m. Simplex optimization does not require a gradient and is most suitable when the optimization problem is not smooth, such as when solving simultaneously for layer conductivity and thickness. The forward solution $f_i(m)$ of Farquharson and Oldenburg (1993) solves for the composite voltage decay curve in a horizontal receiver coil over a 1D layered earth assuming free space dielectric permittivity and magnetic permeability (a dielectric constant of unity and a magnetic susceptibility of zero). The model is typically initialized with the best-fit halfspace, or a layered representation of the L^1 model obtained from EM1DTM (Farquharson and Oldenburg, 1993). The default reference and smoothness weights are zero, such that the inversion is (almost) unconstrained. To enforce positivity of electrical conductivity and thickness, the default lower bound is set according to $\sigma_{min} = 0.01$ mS/m, $L_{min} = 1.0$ m, and $b_{min} = 10^4$. For models with only a few layers, the unconstrained inversion is strictly overdetermined, although imperfect or redundant data may require the use of constraints to obtain a stable solution. Practice shows that for 20-gate ProTEM data, a stable model with more than five layers cannot be recovered without application of significant constraints. Furthermore, recovered models exhibit strong dependence on the initial conditions.

Synthetic Example

Layered inversion results for simple three-layer conductive and resistive synthetic models are illustrated in Figures A1 and A2. The synthetic experiments are 100 m × 100 m central-loop soundings using ten gates at 285 Hz base frequency followed by ten gates at 30 Hz base frequency, both with a 5.1 µs turn-off time. The data are simulated using the forward solution of Farquharson and Oldenburg (1993) and contaminated with 3% random noise.

The conductive model is comprised of a 30 m thick layer of 100 mS/m at 30 m depth in a background of 1 mS/m. The resistive model is comprised of a 30 m thick layer of 0.1 mS/m at 30 m depth in a background of 10 mS/m. In each case, the starting model is a homogeneous model of 10 mS/m. Model recovery is better for the conductive layer as expected. Synthetic results clearly show the difficulty in resolving resistive layers with TEM. Both cases are highly sensitive to initial conductivity and less sensitive to initial model thickness (not shown).

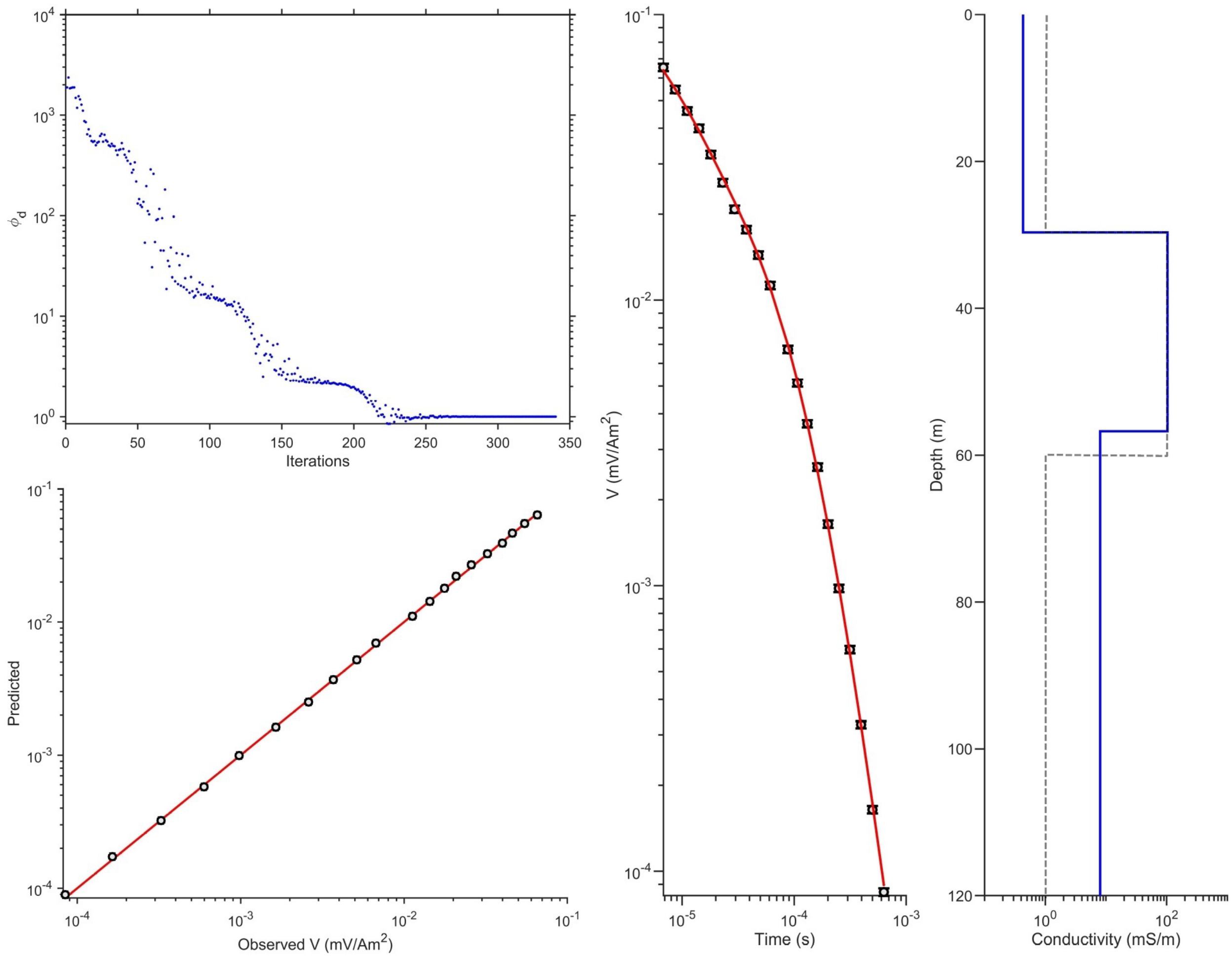

Figure A1. Synthetic inversion results for a conductive layer (gray, dashed) showing the convergence curve for ϕ_d, the predicted versus observed (synthetic) voltage, the predicted and observed (synthetic) decay curve, and the recovered electrical conductivity model. The data are fit to $\phi_d = 1$ with RMSE = 3%, equivalent to the random noise added to the synthetic data.

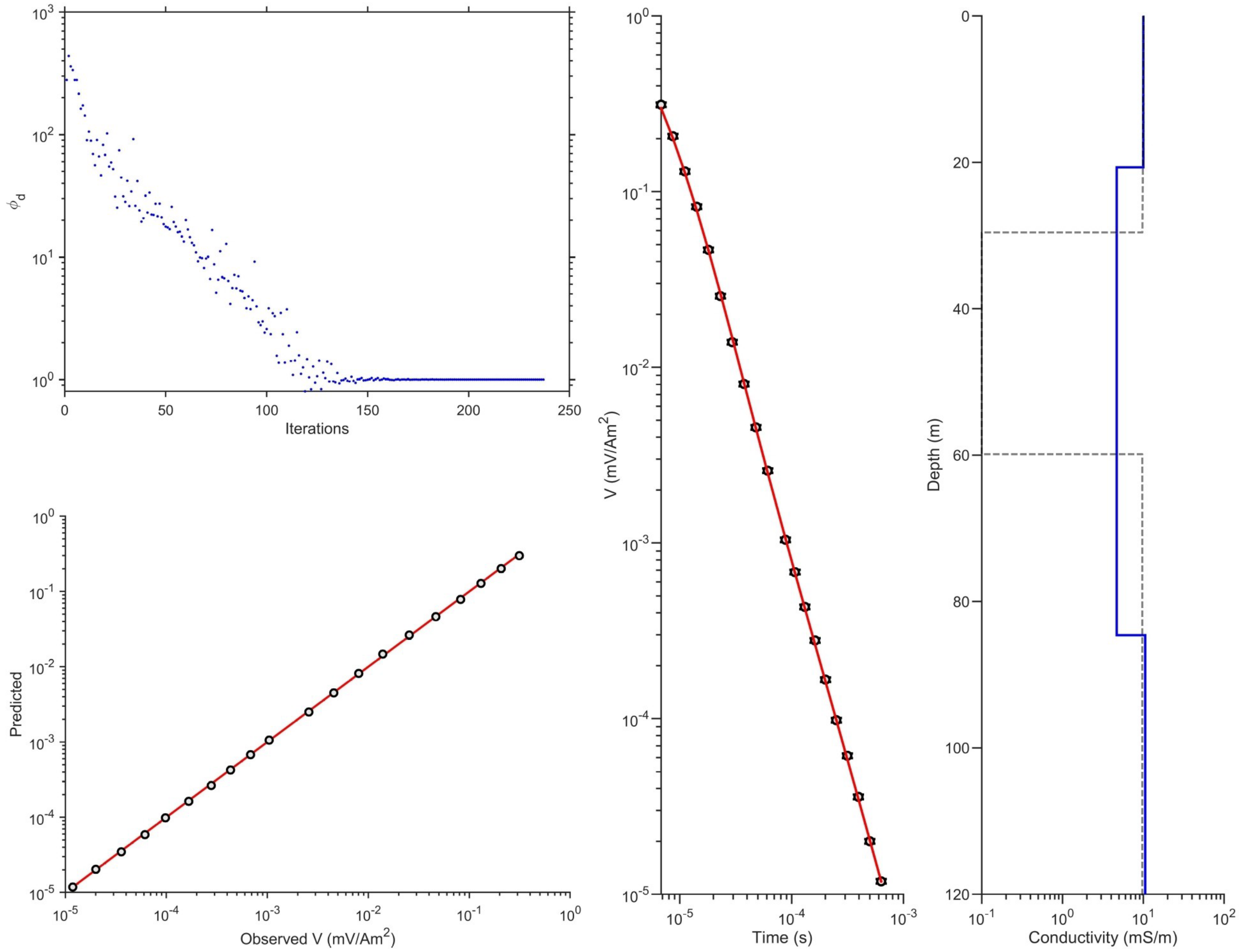

Figure A2. Synthetic inversion results for a resistive layer (gray, dashed) showing the convergence curve for ϕ_d, the predicted versus observed (synthetic) voltage, the predicted and observed (synthetic) decay curve, and the recovered electrical conductivity model. The data are fit to $\phi_d = 1$ with RMSE = 3%, equivalent to the random noise added to the synthetic data.